# Mapping the Active Galactic Nucleus Effects on the Stellar and Gas Properties of NGC 5806

Sophie L. Robbins[1,2] , Sandra I. Raimundo[3,4] , and Matthew A. Malkan[1]

[1] University of Maryland, Department of Astronomy, USA; srobbin7@umd.edu
[2] University of California Los Angeles, Department of Physics and Astronomy, USA
[3] Physics and Astronomy, University of Southampton, UK
[4] DARK, Niels Bohr Institute, University of Copenhagen, Denmark

## Abstract

It is commonly accepted that active galactic nuclei (AGNs) have a strong impact upon the evolution of their host galaxies, but the processes by which they do so are not fully understood. We aim to further the understanding of AGN feeding and feedback by examining an active galaxy using spatially resolved spectroscopy. We analyze integral field spectroscopy of the active galaxy NGC 5806, obtained using the Very Large Telescope Multi-Unit Spectroscopic Explorer. We map the dynamics of gas and stars, as well as gas optical emission line fluxes throughout the central $8 \times 8 \, \mathrm{kpc}^2$ of the galaxy. We use emission line ratios to map gas metallicity and identify regions of gas excitation dominated by AGN/shocks or star formation. We also determine the average stellar population age and metallicity, and model the rotation and dynamics of the galaxy. We find that NGC 5806 has a star-forming circumnuclear ring, with a projected radius of ~400 pc. The dynamics of this galaxy are driven by a large-scale bar, which transports gas from the spiral arm to the central ring and potentially fuels the AGN. We also observe AGN-dominated gas excitation up to 3.3 kpc away from the center of the galaxy, showing the extended AGN effect on the gas in the central regions of the galaxy.

## 1. Introduction

Active galactic nuclei (AGNs) are suspected to influence the formation and evolution of galaxies. Close correlations between supermassive black holes (SMBHs) and the properties of their host galaxies have been established (L. Ferrarese & D. Merritt 2000; K. Gebhardt et al. 2000; A. Marconi & L. K. Hunt 2003; N. Häring & H.-W. Rix 2004; V. N. Bennert et al. 2021), suggesting a coevolution between SMBHs and their galaxies, presumably via gas accretion and star formation regulation by the AGN (A. C. Fabian 2012). The transportation of fuel to AGNs, and feedback from them, have been used in cosmological modeling to explain the evolution of galaxies into what we see in the present Universe (V. Springel et al. 2005; R. S. Somerville et al. 2008; L. Byrne & S. Wellons 2023). However, the means by which AGNs affect and are affected by their host galaxies are still not understood.

Much research has been conducted on specific possible mechanisms of AGN feedback. Winds and radiation pressure from the AGN create outflows, which push gas and dust away from the center of the galaxy (A. C. Fabian 2012). These outflows have been observed in multiple active galaxies (R. A. Riffel et al. 2009; T. Storchi-Bergmann et al. 2010; S. I. Raimundo et al. 2017; P. da Silva et al. 2020; J. H. Costa-Souza et al. 2024), and often move along an ionized bicone centered on the AGN (T. Storchi-Bergmann et al. 2009; G. Venturi et al. 2018). By blowing gas and dust away from the nucleus and potentially out of the galaxy, these

outflows are thought to quench star formation and eventually AGN activity (R. S. Somerville et al. 2008; A. C. Fabian 2012). However, the study of this feedback is complicated by the geometry of AGNs and the different wavelengths of light in which different effects can be observed, so the processes are still under debate.

AGN fueling has been similarly studied, and is similarly not yet fully understood. The inflow of gas along large-scale galactic nonaxisymmetric potentials, such as galactic bars, has been identified as a major factor of AGN fueling. Theoretical studies have found that galactic bars move gas toward the center of their galaxies (M. C. Sormani et al. 2015). This bar-driven gas inflow serves an important role in removing angular momentum from gas, moving it toward the nucleus, and creating a gas reservoir to feed the AGN (L. A. Silva-Lima et al. 2022). However, as L. K. Hunt & M. A. Malkan (1999), K. Wada (2004), and L. A. Silva-Lima et al. (2022) have found, a galactic bar by itself is not sufficient to drive gas all the way to the AGN, and there are many barred galaxies without AGNs. There must be additional factors also at work in feeding the AGN, particularly in the central ⩽100 pc of the galaxy. Several such mechanisms that have been explored in previous studies include galaxy interactions and mergers, gravity-driven turbulence in the gas, dynamical friction between gas clumps and stars, and spiral density waves (K. Wada 2004).

One feature that has been found in many active galaxies is a star-forming circumnuclear ring, often with a radius around 200–500 pc (R. Genzel et al. 1998; G. Dumas et al. 2007; T. Storchi-Bergmann et al. 2007; R. A. Riffel et al. 2009; E. K. S. Hicks et al. 2013; J. H. Costa-Souza et al. 2024). This ring has been theorized to be both a consequence of large-scale gas inflows and a potential source of small-scale AGN feeding;

studies have shown that these rings are formed by inward-flowing gas evolving into a ring due to an inner Lindblad resonance, and that clumps from the ring or the entire ring can collapse inward and feed the AGN (H. Fukuda et al. 2000; K. Wada 2004). Considering how many active galaxies have been found to have this star-forming circumnuclear ring, it is likely that the ring is connected to the AGN in one of three ways: the central ring is either a consequence of the AGN, a consequence of the conditions that trigger an AGN, or a factor itself contributing to triggering the AGN.

In order to determine the interplay between an AGN and its host galaxy, it is important to determine how the gas emission and dynamics of gas and stars vary in different regions of the galaxy. For this reason, integral field spectroscopy has become an important tool for the analysis of active galaxies. Studies such as the Multi-Unit Spectroscopic Explorer (MUSE) Atlas of Disks (S. Erroz-Ferrer et al. 2019), the program from which the data for this paper were obtained, have used spatially resolved spectra in order to distinguish the contributions of AGNs from the effects of star formation, diffuse ionized gas, and other phenomena. We aim to build off of this research and take it a step further, by focusing on one galaxy and thoroughly examining its spatially resolved properties.

This paper is organized as follows. In Section 2, we describe the galaxy examined in this study and the data we use to observe it, and define regions within the galaxy. Section 3 describes the analysis performed on the data in order to measure emission line fluxes and dynamics, and to model the large-scale dynamics of the galaxy. We present the results in Section 4, the discussion in Section 5, and conclusions in Section 6.

## 2. Object and Data

### 2.1. Object

NGC 5806 is a nearby SAB(b) galaxy at $z = 0.00449$, located at R.A. = 15:00:00.47 (J2000) and decl. = 01:53:28.3 (J2000). Throughout this paper, we adopt the cosmology-corrected scale 110 pc arcsec$^{-1}$, from the NASA/IPAC Extragalactic Database (NED).[5] NGC 5806 has an inclination $i = 58°$ and position angle PA = 166° (W. Choi et al. 2023). The total stellar mass of this galaxy has been measured at $\log_{10}(M_*/M_\odot) = 10.59$ (H. Salo & E. Laurikainen 2017), and the diameter is 189″.7.

This galaxy has been classified as a Seyfert 2 galaxy (M. P. Véron-Cetty & P. Véron 2010), and several studies have observed gas with mixed ionization mechanisms, including AGN emissions and star formation (C. M. Carollo et al. 2002; A. Seth et al. 2008; P. B. Westoby et al. 2012; S. Erroz-Ferrer et al. 2019). Multiple studies have found that this galaxy has a large-scale bar, and a circumnuclear star-forming ring (C. M. Carollo et al. 2002; G. Dumas et al. 2007; S. Erroz-Ferrer et al. 2019; W. Choi et al. 2023).

The composite Hubble image in Figure 1 shows NGC 5806 as seen in the optical and infrared (IR) range. The galaxy has a bright center, a central ring, and a large spiral arm with bright clumps. This image also displays several dust lanes, including one that obscures part of the circumnuclear ring. We see more dust obscuration on the left side of this image than the right; therefore, the left side of this image is the near side of the galaxy, and the right side is the far side.
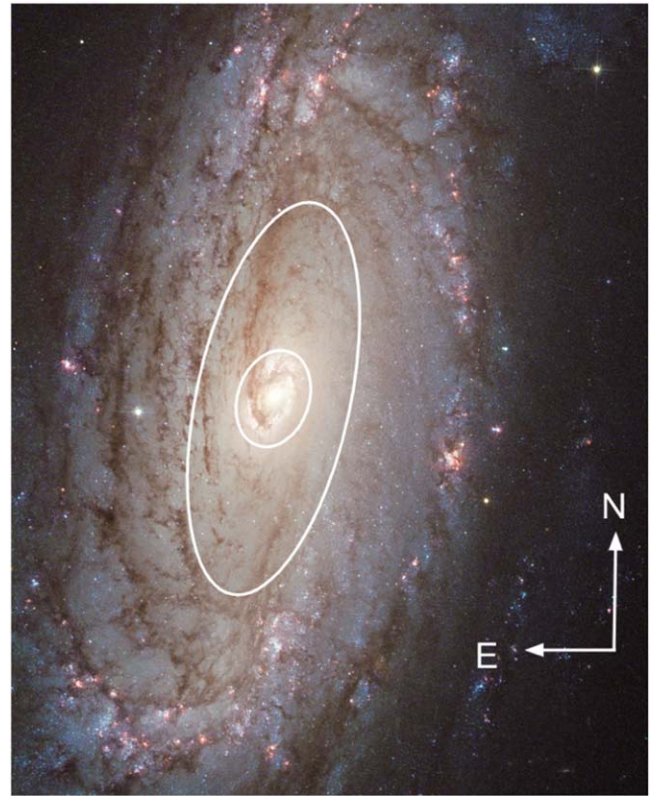


**Figure 1.** Composite Hubble image of NGC 5806, with field of view 1.2 by 1.5. This image combines exposures from the optical filters $B$ (435 nm), $V$ (555 nm), and H$\alpha$ (658 nm), and infrared filter $I$ (814 nm). In this image, one can see supernova SN 2004dg as a yellow spot in the top-right corner. This image clearly shows the dark dust lanes in this galaxy, including a dust lane that stretches toward the center of the galaxy and cuts into the central ring. Two white ellipses are superimposed: the inner ellipse outlines the bright nucleus, which is the same central region, and central ring seen in our MUSE data. The outer ellipse illustrates the approximate location of the galactic bar in this galaxy. Credit: NASA/ESA. Acknowledgment: Andre van der Hoeven.

This galaxy was previously targeted for a supernova SN 2004dg in its outer reaches (N. Elias de la Rosa et al. 2004; A. Vagnozzi et al. 2004; A. H. Harutyunyan et al. 2008). This supernova can be seen in the top-right corner of the Hubble image in Figure 1. However, this supernova, and any effects it may have had, fall outside the scope of our MUSE data, and thus will not be discussed in this paper.

### 2.2. Data

For this paper, we analyze spatially resolved integral field unit spectra, obtained by MUSE on the Very Large Telescope (R. Bacon et al. 2010). These data were originally collected as part of the program "The MUSE Atlas of Disks" (097.B-0165; PI: C. M. Carollo). The image spans a spectral range 475–935.1 nm with 1.25 Å sampling. It has sky coverage 2.2 arcmin$^2$ with ~0″.6 spatial resolution and 0″.2 pixel scale. The galaxy is $22.80 \pm 1.61$ Mpc away, so the data have a physical scale of 22 pc per pixel. These data came from a single exposure, taken with 3600 s of integration, taken on 2016 April 7. We used the Phase 3 data cube that was processed by ESO using the standard pipeline and made available on the ESO archive.[6] For more information on the data reduction, see M. den Brok et al. (2020).
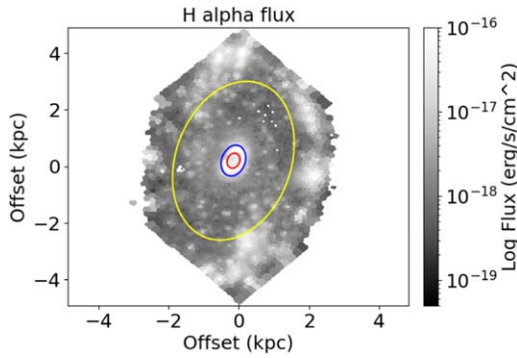
**Figure 2.** A map of Hα emission, with ellipses superimposed to define the regions of the image. In the center, within the red ellipse, is the central region or nucleus. Between the red and blue ellipses is the central ring. The area between the blue ellipse and the yellow ellipse is defined as the intermediate region, and the area outside of the yellow ellipse is the spiral arm. These are a rough definition, meant to aid the reader in understanding the regions referred to for the rest of this paper.

### 2.3. Definition of Regions

In order to clarify terms for the rest of this paper, we define four major regions in our image of this galaxy. These regions are illustrated in Figure 2. The "central region" refers to the center of the galaxy, within a projected radius of ~200 pc. Around this, we have the "central ring," with a projected semimajor axis of ~400 pc and an annular thickness of ~200 pc. At the edge of the image, at a projected distance of ~3000 pc from the center, is a spiral arm. The region in between the spiral arm and the central ring will be referred to as the "intermediate region."

### 3. Data Analysis

We analyzed the data cube to extract the spatially resolved stellar kinematics, gas dynamics, and dominant ionization mechanisms throughout the galaxy. In order to do so, we binned the data, used pPXF to model the spectra of each bin, and used DiskFit to model the disk rotation. Each of these steps will be discussed below.

### 3.1. Voronoi Binning

First, we spatially binned the data, in order to increase the signal-to-noise ratio (SNR). We used the Voronoi binning technique as implemented in M. Cappellari & Y. Copin (2003) to bin spaxels, so that each bin had an SNR ⩾ 50. We took into account the flux uncertainties in each spaxel so that spaxels with high uncertainties or nonphysical values had a lower weighting when binning the data cube. As input to the Voronoi binning, we used the data and error spectra from the data cube in each spaxel. We evaluated the mean SNR in the rest range 6650–6700 Å, where there should be no significant emission lines, in order to evaluate the SNR of the continuum, which was then used for the Voronoi binning. This produced binned spaxels with SNR ⩾ 50. Our final binned data cube contains the average spectrum within each bin.

### 3.2. Fitting Models to Spatially Resolved Spectra

We used the Python package pPXF (M. Cappellari 2023) to fit a model consisting of velocity-broadened stellar templates and emission lines to the spectrum in each bin of the data cube. For this process, we analyzed the spectrum in the rest range 4800–8800 Å, as the spectrum at wavelengths larger than

8800 Å was contaminated with large residuals from sky subtraction.

For stellar templates, we used the XShooter release 2 library of stellar spectra (A. Gonneau et al. 2020).[7] These templates were chosen due to their narrow FWHM, of 0.598 Å, as pPXF requires the stellar templates to have a smaller FWHM than that of the data in order to accurately calculate velocity dispersion. For the instrumental FWHM, we used 2.46 Å, the average of the three FWHM values found for MUSE in S. I. Raimundo et al. (2019).

Before fitting the spectrum, we masked sky lines from N I, ($\lambda$ 5199 Å), Na I ($\lambda$ 5890 and 5986 Å), and O I ($\lambda$ 5577, 6300, 6364, and 6860 Å). We also masked the spectrum from 7200 to 8450 Å, as there were significant residuals from sky subtraction.

To analyze each spectrum, we ran pPXF in two parts. First, it ran with a mask over all of the emission lines, so that it would only be analyzing the stellar continuum. In this step, it found a weighted average of stellar templates, line-of-sight velocity, and velocity dispersion that best fit the data stellar spectrum. This step gave a model for the stellar continuum. Next, the mask over the emission lines was removed. Using the established stellar velocity and dispersion, as well as the weighted templates found in step one, pPXF fit Gaussians to each of the major emission lines: hydrogen transitions Balmer $\alpha$ and $\beta$, (H$\alpha$ $\lambda$6565 Å and H$\beta$ $\lambda$4862 Å), [N II] (doublet around $\lambda$6583 Å), [O III] ($\lambda$5007 Å), and [S II] ($\lambda$6716 and $\lambda$6731 Å). With this model, pPXF calculated the line-of-sight velocity and velocity dispersion of the gas, as well as the flux of each emission line, assuming the same velocity values for all emissions lines. See Figure 3 for an example of a fully modeled spectrum. We ran this two-step process on each bin in the image, in order to create spatially resolved maps of the emissions and dynamics across the galaxy. As discussed below, we then used these emission line fluxes to calculate the gas metallicity and identify sources of gas excitation.

In order to determine properties of the stellar population, we also ran a version of pPXF using the E-MILES stellar library included with pPXF (A. Vazdekis et al. 2016). These templates can be found at MILES.[8] They have an FWHM of 2.51 Å, slightly larger than the average FWHM of our data. Thus they are not ideal for finding velocity and velocity dispersion, and we did not measure stellar velocity or dispersion in this part of the code. However, the MILES templates were sufficient to estimate the stellar population. For this step of the analysis, we masked the same sky lines as before, as well as the emission lines previously listed. The MILES library labels each stellar template with its metallicity $Z = [Fe/H]$, a logarithmic scale where $Z = 0$ is solar metallicity (A. Vazdekis et al. 2010). We edited the MILES library to only include stars with metallicity $Z > -0.5$, in order to match the range of stellar metallicities found in similar local spiral galaxies (J. Neumann et al. 2021). pPXF then found which combination of templates best matched the spectrum for each bin, and from that combination, we were able to calculate the average luminosity-weighted stellar age and metallicity.

When processing and plotting the results from pPXF, we implemented a quality cut by masking pixels with insufficient SNR through two different methods. First, we removed any pixel where the total integrated flux was <0.5% that of the
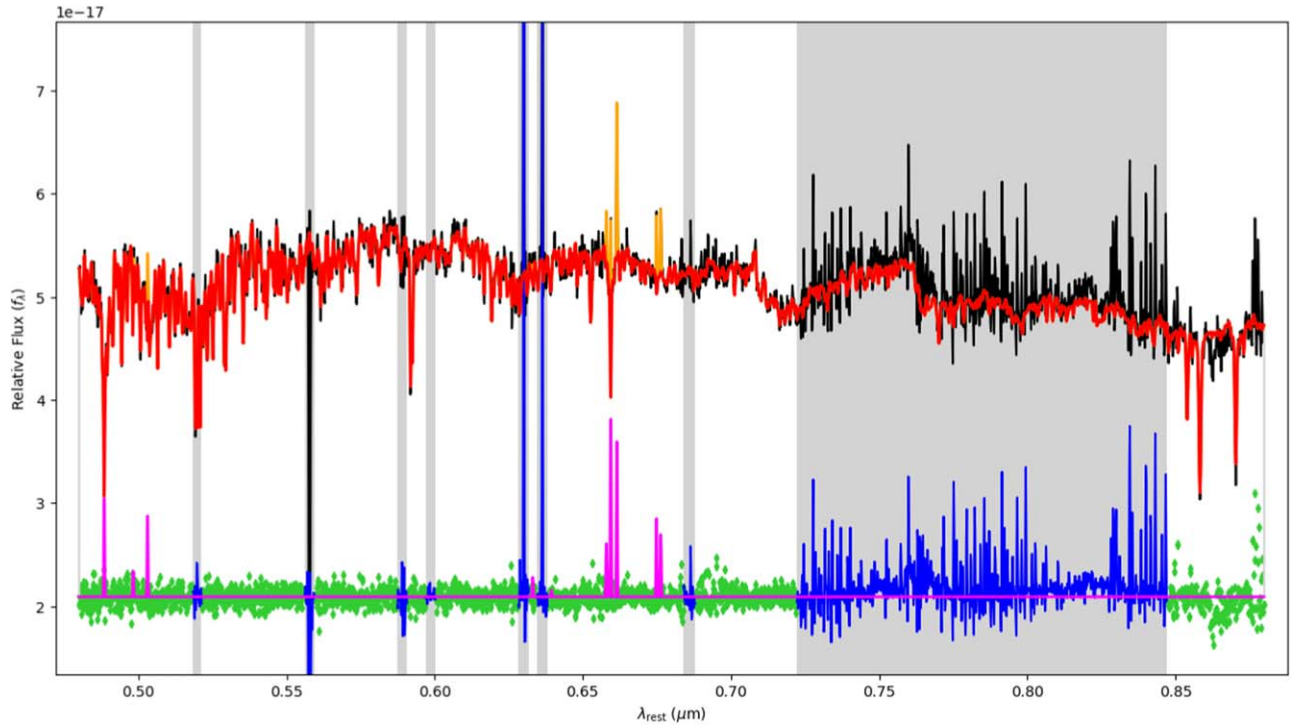
---

**Figure 3.** The integrated spectrum of the center 10 × 10 pixels, or 220 × 220 pc$^2$, of the image, fully modeled using pPXF and the methods described in Section 3.2. In the top line, the black line represents the data spectrum, the red represents pPXF's model of the stellar spectrum, and orange lines model the emission lines. In the bottom portion of the image, green dots illustrate the residuals, and pink lines show the emission lines when seen without the stellar spectrum. Grayed out regions, and the blue lines within, are portions of the spectrum that were masked, and not considered when fitting the model. This spectrum demonstrates the power of pPXF's ability to differentiate gas emission lines from the stellar continuum. For example, in this spectrum, the stellar portion of the spectrum is found to have a deep absorption line at Hα. This enables us to measure a strong Hα emission line, which would not have been visible in this spectrum using the naked eye.

pixel with the maximum total flux in the image. We then also compared the amplitude of the emission lines to the mean amplitude of noise from the binned data cube near the emission line, and removed bins where the amplitude to noise of a line (A/N) was <5. Last, we masked pixels that were dominated by a star in the foreground. We show our results in Section 4.

### 3.3. Modeling Disk Rotation

pPXF allowed us to calculate line-of-sight velocities. We then made further investigation to determine if there were inflows of gas, a kinematically distinct core, or other deviations from simple disk rotation.

To model the rotation of the galaxy, and deviations from a basic disk model, we used the software DiskFit (J. A. Sellwood & K. Spekkens 2015). DiskFit is software that fits disk models to line-of-sight velocity maps, and allows the user to fit models varying from a basic disk to nonaxisymmetric models. It does not fit spiral arms, and assumes that the galaxy has a rotationally flat central disk. DiskFit it built to fit galaxies with nonaxisymmetries such as bars, using photometric or kinematic data. We used the kinematic arm of this code. DiskFit is first described in K. Spekkens & J. A. Sellwood (2007), and the most recent version of the code is explained in J. A. Sellwood & K. Spekkens (2015).

We used DiskFit to fit models to the line-of-sight velocity maps that we found for the gas and stars in this galaxy. For the input data, we used the velocity maps for gas and stars that were outputted by pPXF. Pixels with total integrated flux <0.5% of the maximum flux in the image were set as "not a number," so that they would not be considered in the fit. We fit several models to these data, including a simple disk, radial

flows, warping of the disk, and nonaxisymmetric flows, in order to find the models that produced the lowest minimum $\chi^2$ value. We show the results in Section 4.5.

For each model, we allowed DiskFit to fit the position angle, ellipticity, disk center, inclination, and systematic velocity for each model. We set the seeing correction at 3 pixels, corresponding to the FWHM of our data. We also held several parameters constant in each model, including the starting guesses for parameters, max delta velocity, and the region fit. Another parameter held constant for each model was delta ISM, a parameter in DiskFit's kinematic code that accounts for the velocity uncertainty associated with the turbulence in the interstellar medium (ISM). We set this value to $10 \, \mathrm{km \, s^{-1}}$ for gas and $5 \, \mathrm{km \, s^{-1}}$ for stars, as gas dynamics are more strongly affected by turbulence. We allowed the software to assume that the velocity would rise linearly from 0 at the center of the galaxy, because spaxels close to the center have a high signal level. DiskFit used all of the pixels within a central ellipse with a semimajor axis of 100 pixels, with an ellipticity of 0.3. Outside of this ellipse, DiskFit evaluated pixels in rings, stepping out by 6 pixels for each ring (in order to be double the seeing correction), out to a radius of 165 pixels. When fitting noncircular flow features, we used DiskFit to examine pixels from radius = 3–105, as 105 pixels (~2.3 kpc) were both where we estimated the galactic bar to reach, and the largest radius that caused the nonaxisymmetric model to give physically plausible results.

Once we had created these basic models, we evaluated the residuals and minimum $\chi^2$ value for each model, in order to determine which model best fit our data. We found that the model with $m = 2$ nonaxisymmetric flows, which we will refer

to as the bar model, was the best fit for both stars and gas (See Section 4). From here, we fit the basic disk and bar models to the gas and stars velocity data, this time using bootstrapping, a statistical method in which we fit the model many times, slightly varying the parameters each time, in order to determine uncertainties. We used the bootstrap technique described in J. A. Sellwood & R. Z. Sánchez (2010), with 100 bootstrap iterations. This allowed us to calculate the uncertainties of the parameters output by DiskFit.

# 4. Results

## 4.1. Spatial Distribution of Stars and Gas

With the results from pPXF, we created two-dimensional maps of the dynamics and gas emissions of the galaxy.

Figure 4 includes two-dimensional flux distributions for several major emission lines that trace the ionized gas of the galaxy: $H\alpha$, $H\beta$ [N II], [O III], and [S II]. In all of theses images, there is a bright ring around the center of the galaxy, with a projected radius of ~400 pc. Emission maps also show a larger spiral arm with clumpy bright regions. We observe bright emissions in the very center of the galaxy, especially in [O III].

Figure 5 displays the maps of dynamics in the galaxy. Due to our two-part method of running pPXF, we were able to separate the dynamics of the gas from the stars. Figure 5 shows the stellar line-of-sight velocity, the stellar velocity dispersion, ionized gas line-of-sight velocity, and gas velocity dispersion.

The gas velocity maps show departures from axisymmetry, which is discussed in Section 4.5. Additionally, the circum-nuclear ring that was seen in the emission maps, in the central 800 pc of the image, also appears in the dynamics maps. Here we see that both the stellar and gas components of the ring are rotating around the same axis as the main stellar body, but more rapidly than the ring's surroundings. The dynamics plots also show that the stellar velocity dispersion of the inner ring is lower than that of its surroundings, suggesting the presence of a dynamically cold disk of relatively young stars. The gas velocity dispersion is similarly low within the ring. Just outside the central ring, the gas velocity is significantly greater than it is in the rest of the image. This enhanced gas velocity dispersion reaches farther away from the ring in the northwest direction and southeast. The increased gas velocity dispersion may indicate that the AGN is inducing turbulence in the gas just outside the circumnuclear ring.

## 4.2. BPT Diagrams

We use the commonly used [N II] "Baldwin, Phillips, and Terlevich" (J. A. Baldwin et al. 1981) diagram to identify regions where gas excitation is primarily dominated by AGN excitation, radiation from newly formed stars in H II regions, or a combination thereof (J. A. Baldwin et al. 1981; L. J. Kewley et al. 2006). In this diagram, we plot the [O III]/$H\beta$ flux ratio as a function of the [N II]/$H\alpha$ flux ratio, on the plot seen in Figure 6 (left). The solid blue line represents the extreme starburst boundary line from L. J. Kewley et al. (2001), while the dashed green line shows the G. Kauffmann et al. (2003) pure star formation track. Points that fall above and to the right of both of these lines are classified as AGN-dominated, while points to the left and below the G. Kauffmann et al. (2003) line are marked as star-formation-dominated. Points in between the two lines are classified as composite, potentially with an

excitation contribution from the AGN, star formation, shocks, or a combination thereof.

Using the emission lines previously discussed, we plotted each bin of the image on an [N II] BPT diagram, and then mapped the spatially resolved results back to the physical regions of the galaxy (see Figure 6, right). Pixels were removed from this map if any of the four emission lines used did not each have the required SNR and total flux threshold, as discussed in Section 3.2. This BPT map indicates that the inner circumnuclear ring and the outer spiral arm are H II regions, primarily ionized by star formation. It also shows that gas at the center of the galaxy, and in the intermediate region, is primarily excited by the AGN. This excitation from the AGN reaches up to 3500 pc away from the center of the galaxy. This is the same trend seen in other spatially resolved maps of line emission in Seyfert 2 galaxies (J. Xia et al. 2018). In the case of high O III/$H\beta$ (Seyfert) regions, the mechanism is believed to be photoioniza-tion by the hard AGN continuum photons. In the case of the high [N II]/Halpha (LINER) regions, it is possible the energy transfer is mechanical, perhaps in the form of an outgoing wind.

## 4.3. Gas Metallicity

Next we calculated the gas metallicity, from the [O III]/$H\beta$ and [N II]/$H\alpha$ line ratios and the O3N2 metallicity calibration for H II regions from R. A. Marino et al. (2013). We calculated the O3N2 metallicity of the inner and outer rings, where the BPT diagram indicates that there are H II regions (Figure 7, left). In these images, as in the BPT maps, we remove pixels where any of the diagnostic emission lines have SNR < 5. We also remove any pixels where the Balmer decrement is measured to be <2.86, the theoretical Balmer ratio (D. E. Osterbrock & G. J. Ferland 2006), to avoid pixels where the Balmer decrement is unphysical. We also calculated the metallicity of gas in regions excited by the AGN, as indicated by the BPT map, using the [N II] calibration from S. P. Carvalho et al. (2020), which was calibrated for AGN-excited regions (Figure 7, right).

The results from both calibrations indicate that there is no significant metallicity gradient in the disk of this galaxy. In the H II regions of the central ring and the outer spiral, the gas metallicity stays at and slightly above the solar metallicity, 8.69 (M. Asplund et al. 2009). Similarly, in the central region, the gas metallicity is near solar metallicity. The gas metallicity is slightly higher in the intermediate region, but never goes above 2 times solar metallicity. Figure 7 shows maps of gas metallicity throughout the image, with the H II calibration on the left and the AGN calibration on the right.

## 4.4. Average Stellar Population

To determine the average properties of the stellar population, we use the results from pPXF to map the average stellar age and metallicity, displayed in Figure 8. These images show that the central ring is primarily made up of relatively old, low-metallicity stars. This ring is surrounded by a region of younger, higher-metallicity stars. This ring of relatively old stars is unexpected, as it is cospatial with regions that the BPT diagram marked as locations of star formation.

In order to test the statistical significance of the stellar population results, we ran the central ring and the intermediate region through a Monte Carlo simulation. In this simulation, we ran pPXF on the spectrum of each pixel 200 times, varying the starting parameters slightly each time, in order to
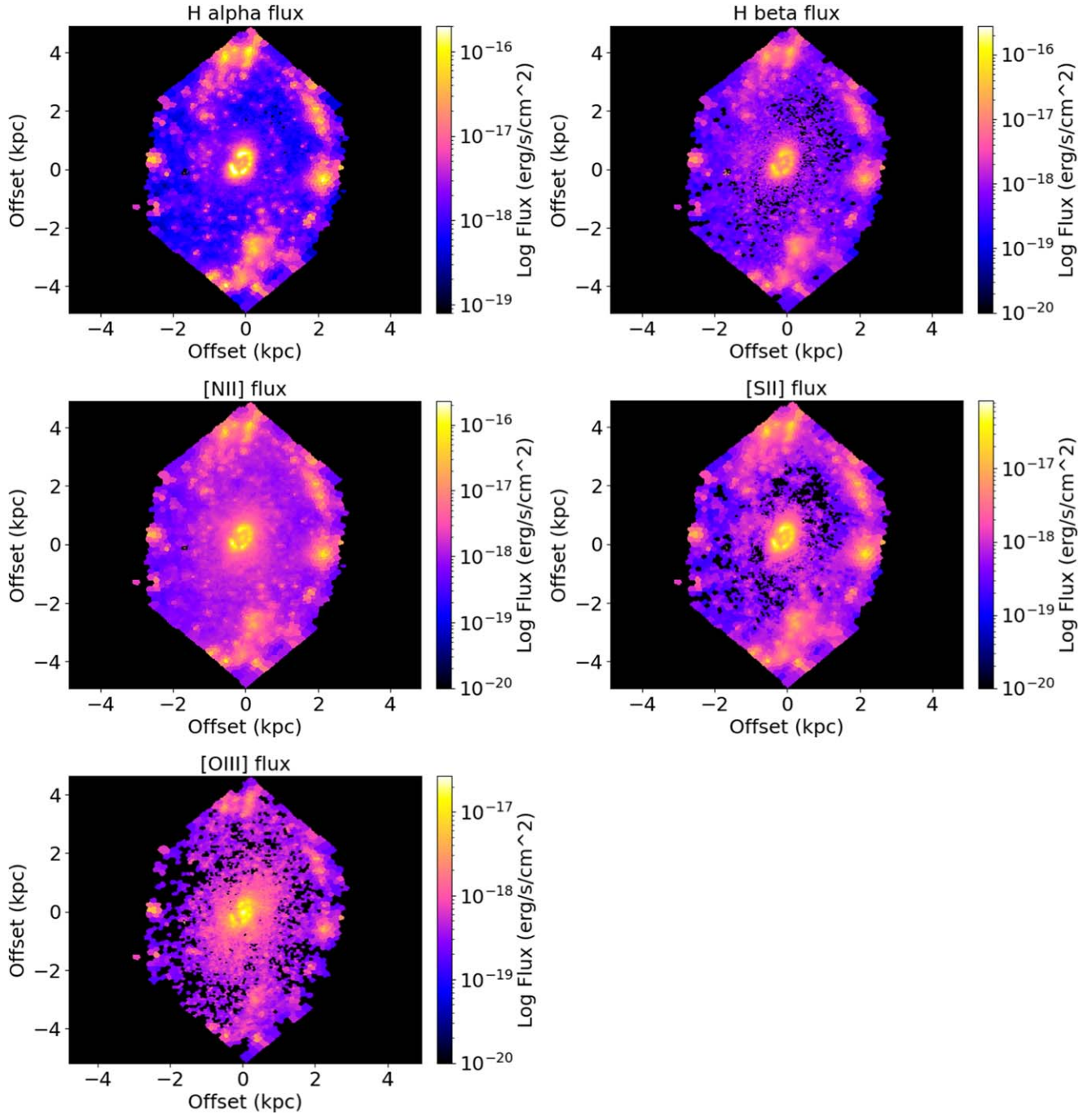
**Figure 4.** Two-dimensional flux maps of the major emission lines observed in the optical range: Hα, Hβ, [N II], [S II], and [O III]. The black pixels in these images are bins that were removed because the signal-to-noise ratio of the emission line was <5, or the total flux was <0.5% of the maximum flux of the image. In these and all other images created from the MUSE data cube, north is up and east is left.

find the uncertainties of the output parameters. The results of this Monte Carlo test are listed in Table 1. We find that there is a $>1\sigma$ difference in age and metallicity between the circumnuclear ring and the surrounding area. Therefore, we tentatively find that the stars in the central ring are relatively old and low-metallicity, but these results are not statistically significant.

### 4.5. Modeling Dynamics with DiskFit

In order to better understand the dynamics of this galaxy, we used the software DiskFit to fit several models to our stellar and

gas velocity maps. (See Section 3.3 for more details on DiskFit.) The first model that we tried was basic disk rotation. In Figure 9, we display the stellar and gas line-of-sight velocities, basic disk model, and residuals. In the residuals from this basic model, for both the stars and gas, we see large, antisymmetrical residuals in the central $1 \times 1 \, \text{kpc}^2$ of the galaxy (see the rightmost panels in both rows of Figure 9). This type of residual has been found by L. Lin et al. (2022) to indicate the presence of a galactic bar. We also see an S-shaped distortion in the line-of-sight velocity map for gas, illustrated in Figure 10. This S-shape was also identified by L. Lin et al.
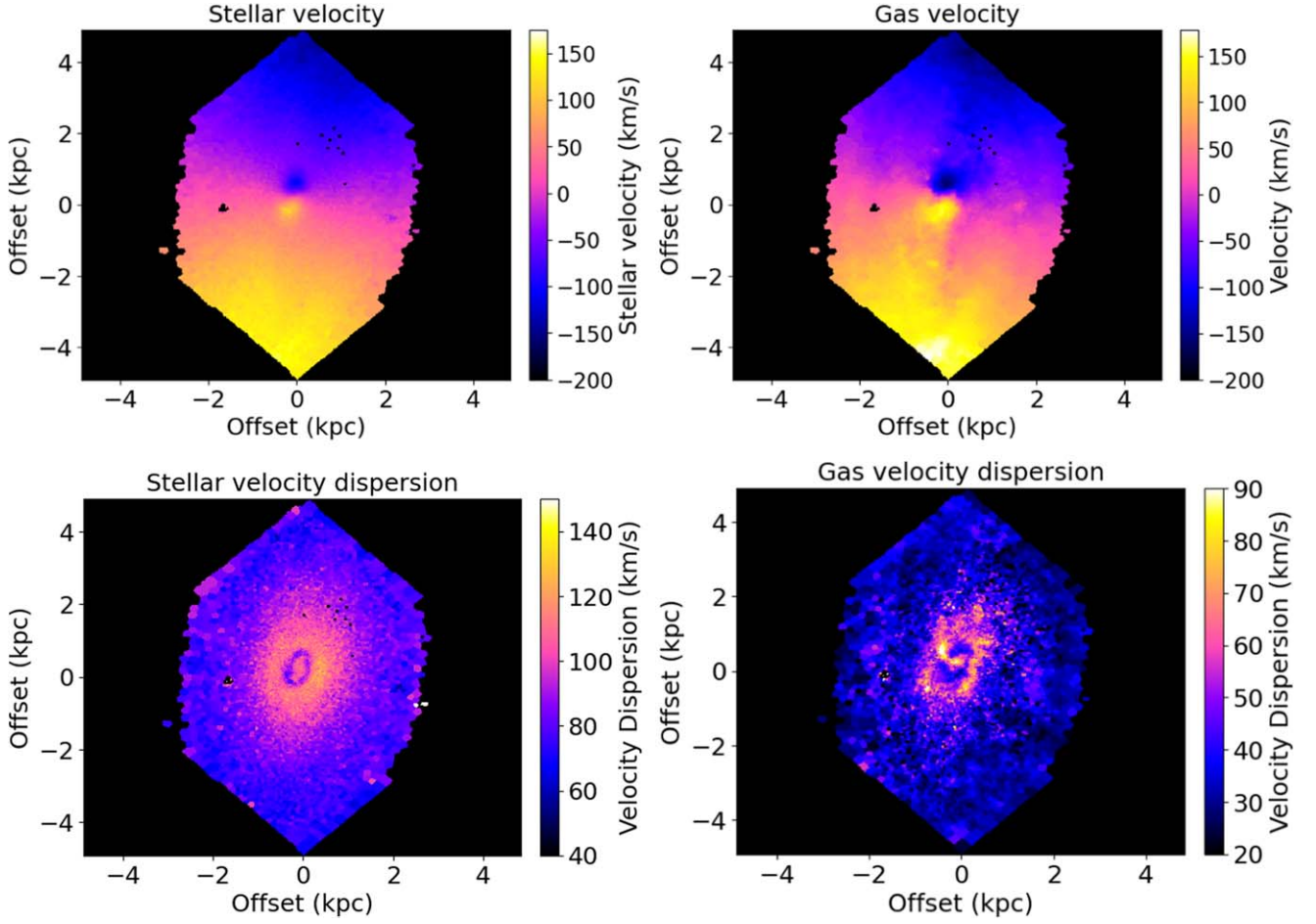
**Figure 5.** Two-dimensional maps of stellar (left column) and gas (right column) dynamics. Line-of-sight velocity is shown at the top and velocity dispersion at the bottom. North is up, east is left. The small masked region in black, on the left-hand side of each map, corresponds to a star in the foreground, which was removed from all final maps.
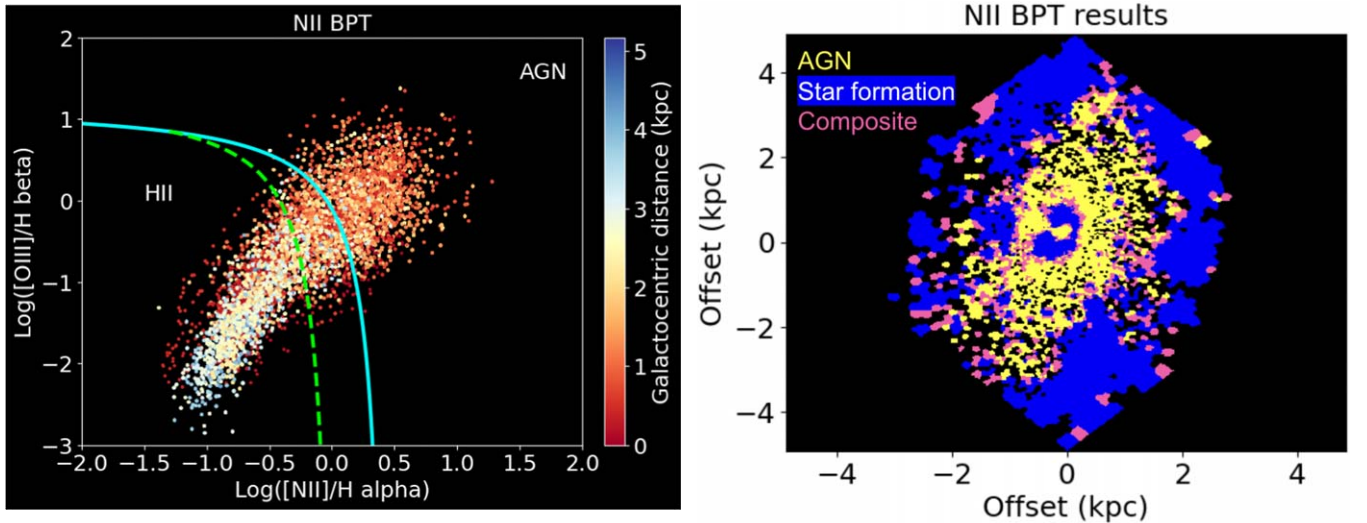


**Figure 6.** Left: the NII BPT diagram, with each spaxel plotted individually, using emission line ratios to categorize each bin in the image by its main source of gas excitation. Points that fall to the right of the solid blue line indicate gas dominated by AGN excitation, while points to the left of the dashed green line indicate an H II region. Points that fall between the two lines are classified as composite. The color bar indicates the spaxel's distance from the center of the galaxy, in kiloparsecs. Right: the results from the BPT diagram—that is, which section of the BPT diagram each spaxel lands within—are then mapped on the right panel over the image of the galaxy. Yellow pixels indicate AGN excitation, blue pixels mark star-forming H II regions, and pink pixels are composite.

(2022) as a signature of bar-driven kinematics. Therefore, we explored several other models available through DiskFit, in order to find a better model for our data.

After the basic disk showed signs of nonaxisymmetry, we tried several different models: a warped disk, radial flows, and nonaxisymmetric flows with $m = 1$ and $m = 2$. The
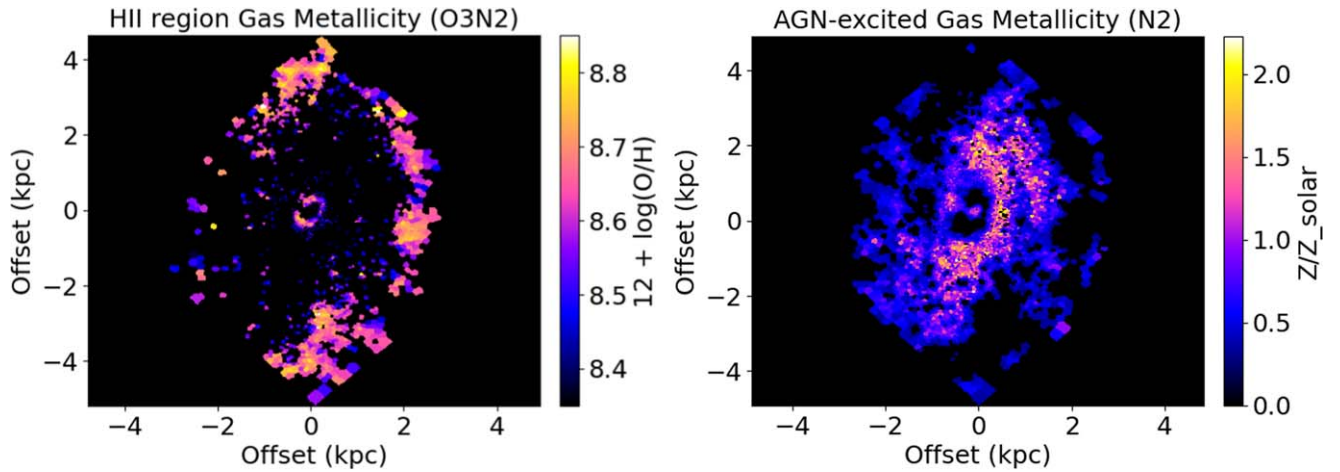
**Figure 7.** Left: gas metallicity calculated using the O3N2 calibration for H II regions from R. A. Marino et al. (2013), mapped in BPT-identified H II regions. The metallicity remains close to solar values throughout the image, with no visible gradient. Right: metallicity of gas in regions excited by the AGN, using the N2 calibration for AGN regions from S. P. Carvalho et al. (2020).
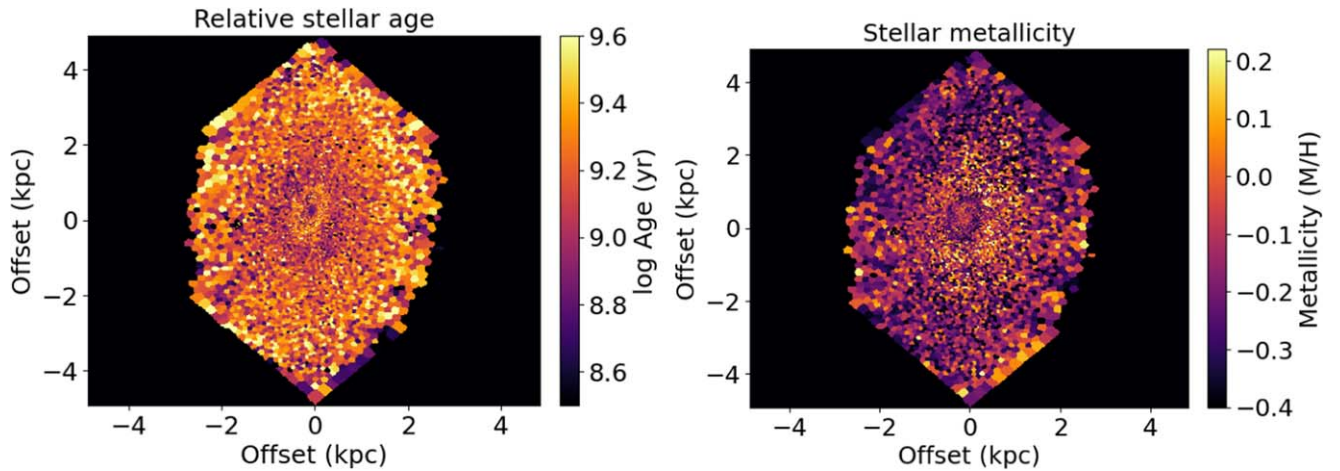


**Figure 8.** Left: average stellar age. Right: average stellar metallicity. As in the full gas and stellar fit, we removed pixels where the total integrated flux was <0.5% of the max integrated flux in the image. The stars in the central ring and spiral arm are somewhat relatively old and low-metallicity, while the youngest and highest-metallicity stars seem to appear in the central and intermediate regions.

**Table 1**
Mean Stellar Age and Metallicity in the Central Ring and the Intermediate Region

|  | Central Ring | Intermediate Region |
|---|---|---|
| Mean age (log yr) | $9.43 \pm 0.02$ | $9.08 \pm 0.20$ |
| Mean metallicity (M/H) | $-0.33 \pm 0.01$ | $-0.10 \pm 0.16$ |

**Note.** Both regions were run through a Monte Carlo simulation to test the statistical significance of the findings. The stellar population of the central ring seems to be older and lower metallicity than the population of the intermediate region, but these results are within $1\sigma$ of each other and thus not statistically significant.

nonaxisymmetric flow patterns are modeled using summations of $\cos(m\theta)$; for more details, see K. Spekkens & J. A. Sellwood (2007). We found that a disk with nonaxisymmetric flows at harmonic order $m = 2$ was the model that best fit the data and produced the lowest minimum $\chi^2$ value, for both gas and stars. This model was built to fit barred spiral galaxies, and thus we will refer to it as the bar model (J. A. Sellwood & K. Spekkens 2015; see Figure 11 for an illustration of the bar model). Therefore, in agreement with the residuals that we observed in

the basic disk model, the nonaxisymmetric distortion in NGC 5806 is best explained by the presence of a bar. With this model, we found the parameters listed in Table 2.

The bar model fits the observations significantly better than the basic disk model. This can be seen in the reduced structure in the residuals of the bar model, as compared to the antisymmetric residuals from the basic disk model (see Figures 9 and 11). The bar model also has lower $\chi^2$ values than the basic disk model, for both gas and stars, as shown in Table 3. We limited the length of the bar to 105 pixels, as this was what we estimated using the Hubble image in Figure 1, and this size of bar—2.3 kpc in radius —gave the best fit for the DiskFit model. There is still some structure in the residuals of the stars and gas velocity, with positive residuals in the top-left and bottom-right side of the image, and negative residuals in the top right and bottom left; however, this can be explained by the presence of the spiral arm, which the DiskFit model does not include.

In addition, we ran DiskFit on the inner $2 \times 2 \, \text{kpc}^2$ of the galaxy, in order to test if the inclination or position angle of the central ring might differ from that of the major disk of the galaxy. We found no such discrepancy; the central ring is aligned with the major gas disk of the galaxy.
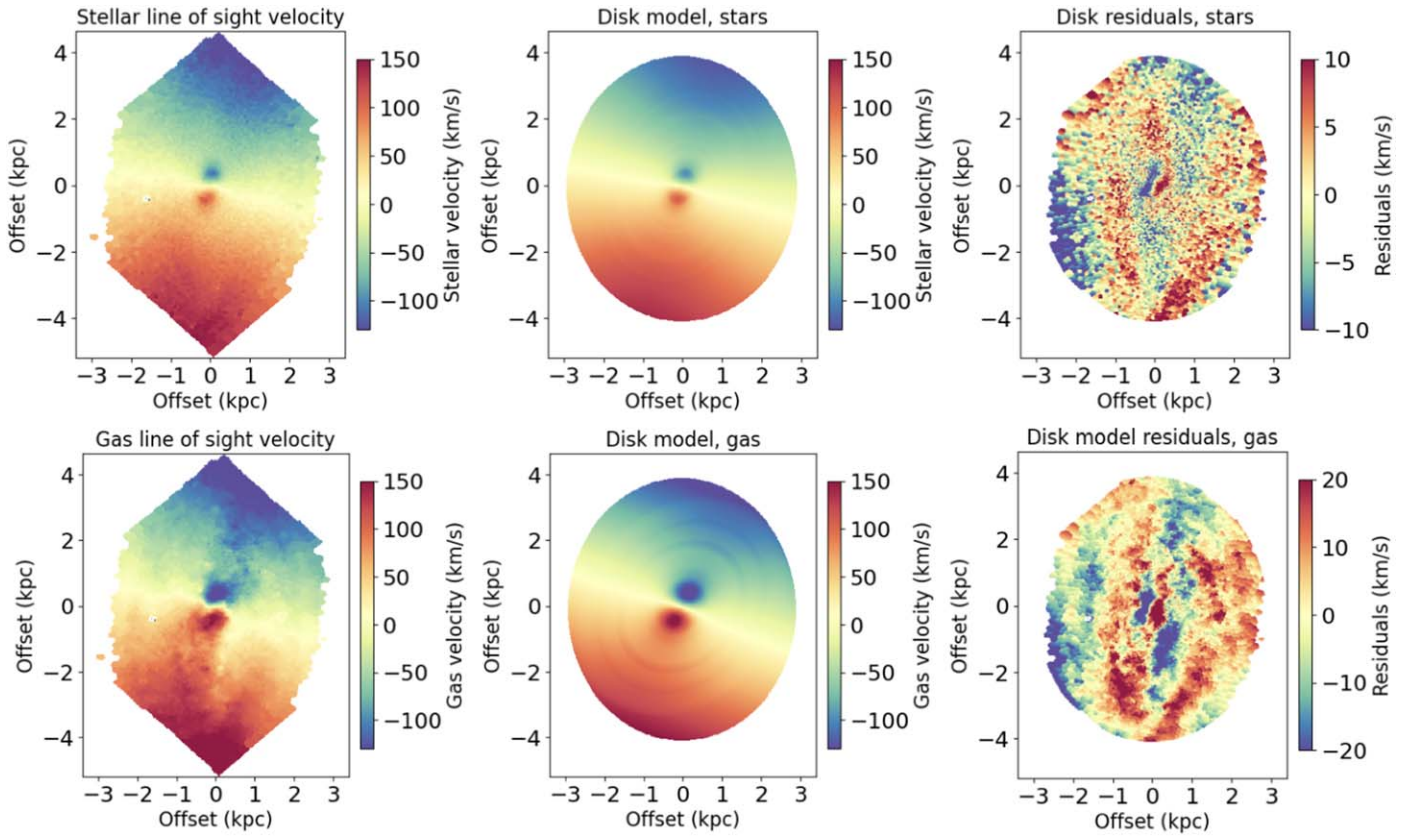
**Figure 9.** Maps of DiskFit modeling, fitting a basic disk model to the stellar and gas velocity. The top row, from left to right, includes the stellar velocity map output by pPXF, a model fitting this velocity data as a basic disk, and the residuals from subtracting this model from the data. The bottom row includes the same maps, but for gas rather than stars.
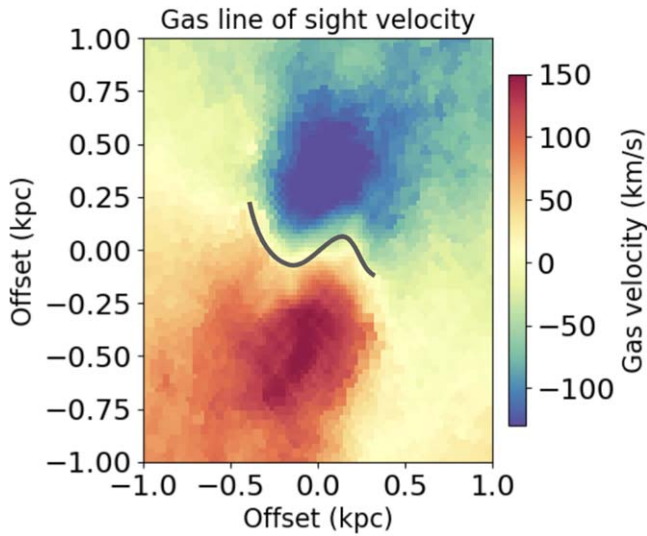


**Figure 10.** Line-of-sight velocity of gas in the center $1 \times 1$ kpc$^2$ of the galaxy, with the S-shaped distortion illustrated. This distortion indicates the presence of a galactic bar.

### 4.6. Maps of the Central Ring

We present the maps previously featured, zoomed-in on the central ring, in Figure 12. The blue ellipses are superimposed so that the viewer can compare the location of the ring in each image. These images show that the ellipse visible in each map is in fact the same central ring. This indicates that the maximum gas emissions and oldest and lowest-metallicity stars

in the image all occur in the same space, which has been identified as H II regions. This ring is also a location of high stellar and gas velocity, and low stellar and gas velocity dispersion. Normally, this low-velocity dispersion would indicate the presence of newly formed stars, as would be expected in H II regions; however, our analysis of the stellar population instead indicates that the average stellar age in this ring is relatively old compared to the regions around it. This ring has a projected radius of about 400 pc. Potential reasons for this discrepancy will be discussed in Section 5.

### 5. Discussion

#### 5.1. AGN-dominated Emissions

With the quality of data provided by MUSE, we have been able to measure the gas excitation mechanisms of different regions of this galaxy with great detail. S. Erroz-Ferrer et al. (2019) found that the central region of this galaxy showed signs of AGN excitation, a finding that we have confirmed. In addition, due to our method of increasing the SNR through Voronoi binning, we also find significant AGN emissions in the intermediate region, reaching over 3 kpc away from the AGN. The reach of these emissions suggests that the AGN may be affecting the gas in this galaxy up to greater distances than previously observed.

#### 5.2. Central Ring

In the center of this galaxy, we see a star-forming central ring with a projected radius of approximately 400 pc. This star-forming ring has been observed by several previous studies
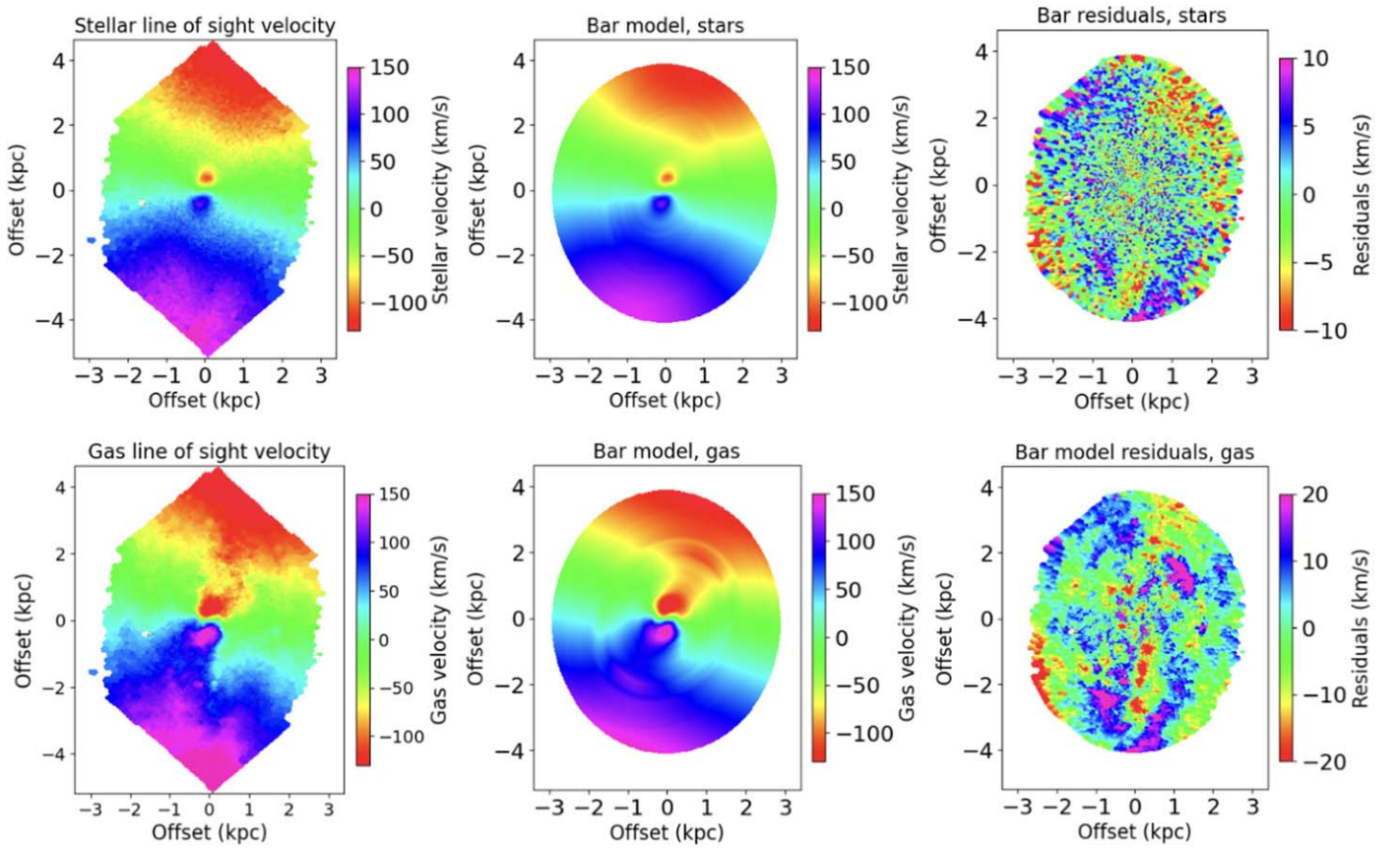
**Figure 11.** Maps of DiskFit modeling with the bar model. This model fits the data better than the basic disk model. The top row shows the stellar line-of-sight velocity, bar model, and the residuals from this model. The bottom row contains the same maps, but for gas.

**Table 2**
Best-fit Parameters from DiskFit for a Model with a Galactic Bar, Modeling Velocity Maps of Gas and Stars

|  | Stars | Gas |
|---|---|---|
| Disk PA | −12.2 ± 0.5 | −19 ± 1 |
| Ellipticity | 0.41 ± 0.02 | 0.28 ± 0.04 |
| Inclination | 54 ± 1 | 44 ± 3 |
| Bar PA | 104 ± 4 | 69 ± 5 |

**Note.** Position angle and inclination are in units of degrees. The ellipticity and the position angle (PA) of the disk and the bar are notably different for the gas and stars.

**Table 3**
$\chi^2$ Values for the Basic Disk Model and Bar Model, When Compared to Line-of-sight Velocity Maps for the Gas and Stars of This Galaxy

|  | Stars | Gas |
|---|---|---|
| Basic Disk | 1.22 | 1.83 |
| Bar | 0.88 | 0.85 |

**Note.** These $\chi^2$ values enable us to compare the bar model to the disk model, and show that the bar model is a better fit.

(C. M. Carollo et al. 2002; G. Dumas et al. 2007; S. Erroz-Ferrer et al. 2019; W. Choi et al. 2023). We find that this ring has a high concentration of excited gas, and lies in the H II region zone on a BPT diagram.

We have also shown that this ring rotates distinctly from the rest of the galaxy, with rapid rotation and low velocity dispersion. These dynamics show elevated rotational support consistent with a dissipative formation channel, such as gas inflow accumulation caused by a bar. In addition, the ratio of the ring-to-bar size falls within ranges previously found for nuclear disks fueled by bars. The size of the ring is ~0.17 times the radius of the bar. This is slightly larger than the values found by D. A. Gadotti et al. (2020) for the typical sizes of nuclear disks formed by bars, and slightly lower than the predicted theoretical value of 0.3 (D. R. Cole et al. 2014).

In all of the emission line maps that we have created, we see that there is a gap in the northeast portion of the ring. Based on the Hubble image in Figure 1, we believe that this portion of the ring is merely obscured by a dust lane, which would explain the gap observed. In order to test this, we found the amplitude of the Hα and Hβ lines within an integrated spectrum for this region. We calculate the Balmer decrement in the gap in the ring to be 7.3. This falls on the high end of Balmer decrement values measured by K.-X. Lu et al. (2019) in the central regions of active galaxies. Therefore, we find that there is a significant amount of dust in this portion of the ring.

To view this region without the dust lane blocking our view, we reference the infrared image displayed in Figure 13. This image was taken by Hubble Space Telescope's Near Infrared Camera and Multi-Object Spectrometer (NICMOS), in the central $R \approx 15'$ of NGC 5806. There is a ~3″ offset in coordinates between this NICMOS image and our MUSE data, as can be observed by interpreting the brightest point in the IR image to be the AGN. This image reveals a reservoir of dust within the central region, which may contribute to feeding the
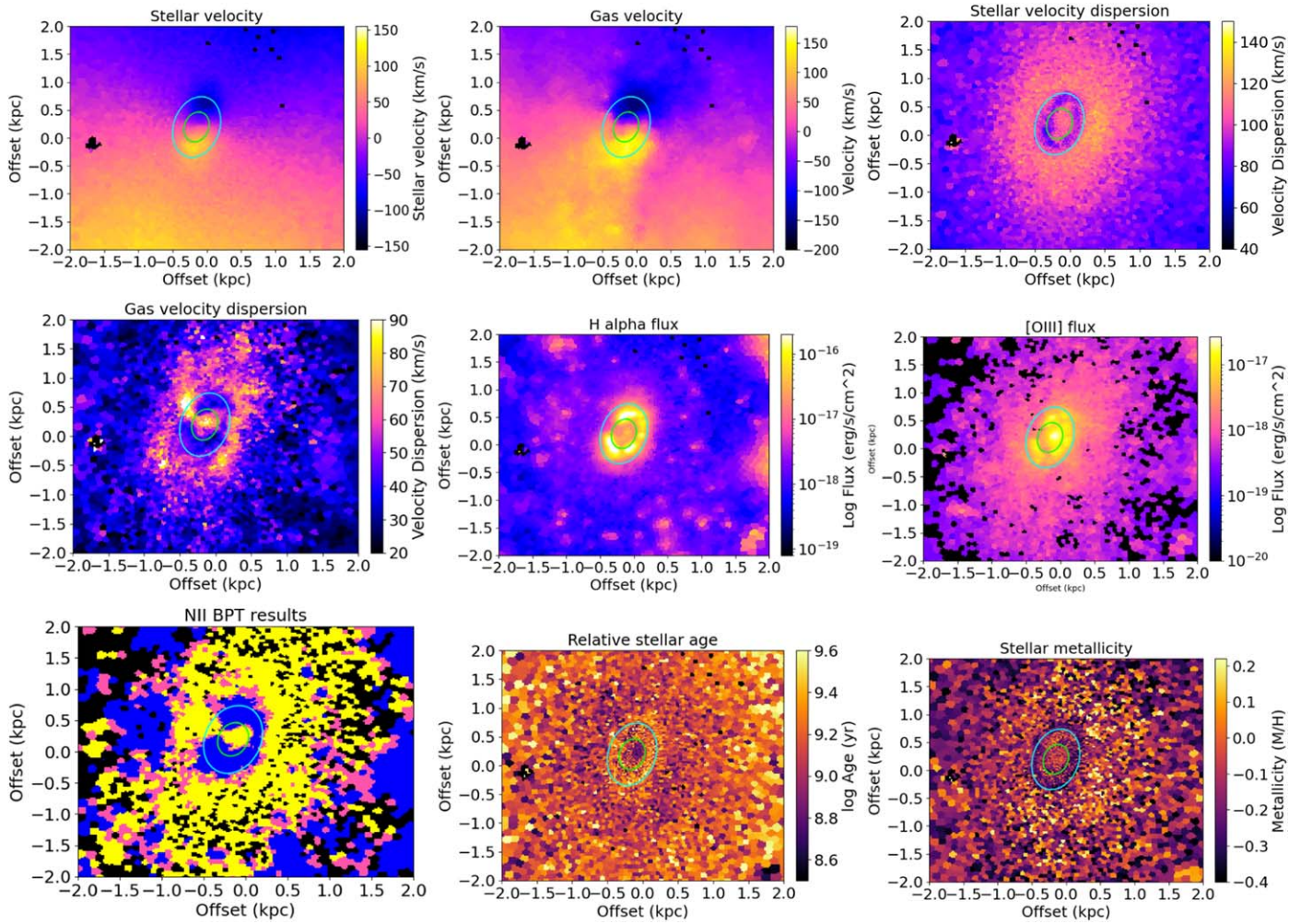
**Figure 12.** Maps of stellar velocity, gas velocity, stellar velocity dispersion, gas velocity dispersion, H$\alpha$ flux, [O III] flux, results from the BPT diagram, average stellar age, and average stellar metallicity, all zoomed-in on the central 2 kpc$^2$ of the galaxy. Ellipses are superimposed in the same location in each map, in order to demonstrate that all of the effects that we observe are cospatial.

AGN. Another interesting feature of this image is that the southern portion of the central ring resembles a spiral arm, which could potentially warrant further investigation.

More pertinently to this portion of the discussion, the NICMOS image shows the circumnuclear ring to be largely unbroken in the northeast. Therefore, it is likely that the physical ring does not have a gap in it. The gap in optical emission, however, could still be of interest.

The gap in optical emission could be in part due to the inflow of gas disrupting star formation. At the same location where we see the gap in optical gas emission, we also find high gas velocity dispersion breaking into the circumnuclear ring. W. Choi et al. (2023) found that this part of the ring is where a bar-driven gas inflow connects with the central ring. They found high molecular gas velocity dispersion in this node, similar to what we find. This increased velocity dispersion, seen in both molecular and ionized gas, could disrupt star formation, which would in turn decrease ionized gas emissions. This would explain why this portion of the ring is not marked as an H II region according to the BPT diagram. We also find that the gas velocity dispersion on the opposite (right) side of the ring, where W. Choi et al. (2023) found another node, is somewhat increased when compared to the rest of the circumnuclear ring. However, we do not see a matching gap

in the ring emissions on the right side, so there may be more complicated effects at play.

### 5.3. Fueling the Central Ring and AGN

Evidence from our models of the gas dynamics, and previous research by W. Choi et al. (2023), indicates that the central ring is likely fueled by gas inflows driven by the bar.

We find that the dynamics of this galaxy are dominated by a rotating disk and a bar. When we fit the line-of-sight velocity maps with a simple disk model, the residuals resembled those found by L. Lin et al. (2022). They found an S-shaped zero-velocity isophote and antisymmetric residuals at the center in multiple barred galaxies; and, we see both of those features in NGC 5806 (see Figure 10). Furthermore, the bar model was the best fit for the velocity fields of this galaxy. We find no evidence of other phenomena or structures significantly affecting the dynamics of this galaxy, aside from potentially the spiral arm. Therefore, we find that the bar of this galaxy has a significant impact on its dynamics.

Previous studies have found that galactic bars cause galactic inflows toward the galactic center (M. C. Sormani et al. 2015). Therefore, we conclude that in NGC 5806 (a galaxy that we find to be dynamically dominated by the movement of a galactic bar), there is a bar-driven inflow toward the center of
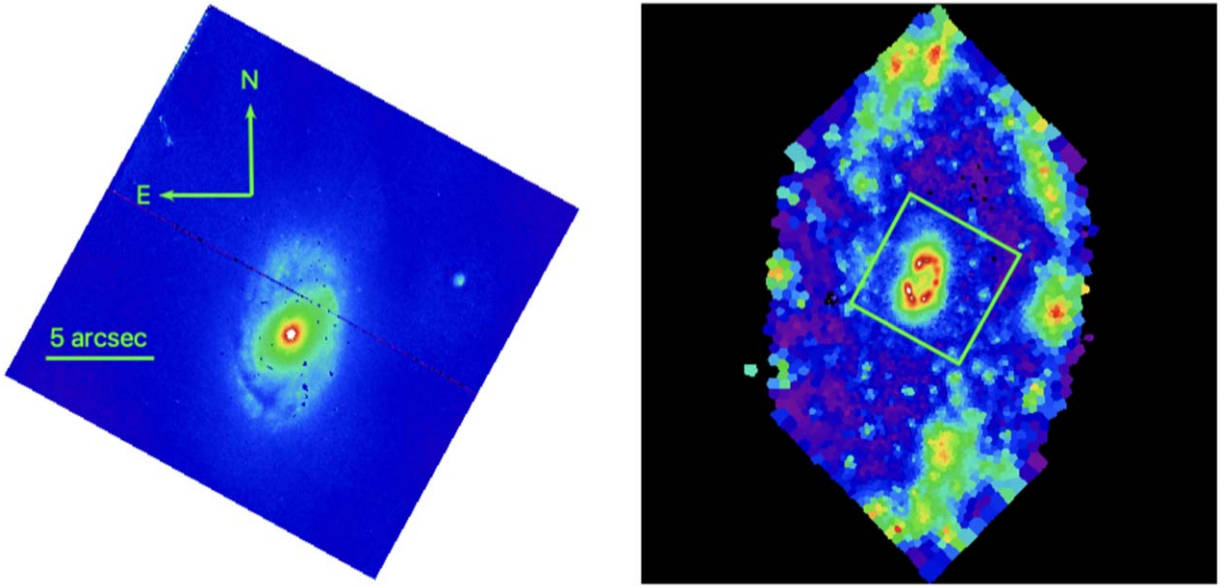
**Figure 13.** Left: infrared image of the center of NGC 5806, taken by Hubble Space Telescope's Near Infrared Camera and Multi-Object Spectrometer (NICMOS). This image was taken with NICMOS' F110W filter, on 1998 February 2 (HST Proposal ID #7331, PI: M. Stiavelli 1997; Carollo et al 1998). There is a ~3″ offset in coordinates between this NICMOS image and our MUSE data. The brightest point in this image is the AGN, and the ellipse pictured is cospatial with the central region and circumnuclear ring seen in the optical. Right: Hα map from MUSE data cube, with the field of view of the IR image superimposed in green for scale reference.

the galaxy. This inflow likely provides fuel for the star formation in the central ring.

Beyond the dynamics of the bar, we observe several other pieces of evidence supporting the existence of a bar-driven gas inflow. As previously discussed, both our observations and W. Choi et al. (2023) find increased gas velocity dispersion in the northeast and southwest portions of the central ring. W. Choi et al. (2023) found evidence that these two areas of high velocity dispersion are caused by gas inflows driven by the bar into the central ring, with velocity $V_{in} \approx 120 \, \text{km s}^{-1}$ and a total mass inflow rate of $5 \, M_{\odot} \, \text{yr}^{-1}$.

It is very difficult to estimate the AGN accretion rate. One common method is to infer the accretion-produced bolometric luminosity, which has been attempted by multiplying the hard X-ray luminosity by an approximate correction factor of 10. According to S. D. Connolly et al. (2016), the 2–10 keV luminosity is $8 \times 10^{39} \, \text{erg s}^{-1}$, and this observation by SWIFT is consistent with the average of several XMM observations from the 4XMM-DR13 stacked catalog (xsa.esac.esa.int/nxsa-web/). Multiplying the hard X-ray luminosity by a factor of 10 gives a bolometric luminosity of $8 \times 10^{39} \, \text{erg s}^{-1}$, which for an accretion efficiency of 0.1, corresponds to an extremely low mass consumption rate of $10^{-6}$ solar masses $\text{yr}^{-1}$. The Hard X-ray bolometric correction assumed by L. Spinoglio et al. (2024) would give an accretion rate several times higher. However, if we were instead to scale from the $12 \, \mu\text{m}$ flux detected by WISE (Band 3, assuming that the active nucleus dominates the total), then the L. Spinoglio et al. (2024) relations would lead to an accretion rate more than an order of magnitude larger.

Using the Hα flux, we calculate the star formation rate (SFR) in the center $1 \times 1 \, \text{kpc}^2$ of the galaxy. We use the calibration from R. C. Kennicutt (1998):

$$\text{SFR}(M_{\odot} \, \text{yr}^{-1}) = 7.9 \times 10^{-42} L(\text{H}\alpha)(\text{erg s}^{-1}). \quad (1)$$

This calibration does not account for the presence of the AGN, and is often limited in circumnuclear regions due to dust

attenuation (R. C. Kennicutt 1998). Therefore, we include this calculation only as an estimate and lower boundary on the star formation rate. In the nucleus and central ring of this galaxy, we find that the total star formation rate is $0.06 \, M_{\odot} \, \text{yr}^{-1}$. This SFR falls within the range of SFRs found by L. M. Mazzuca et al. (2008) in their study of star-forming rings.

The gas metallicity of the galaxy provides further evidence for the inflow of gas to the central ring. We find that the gas metallicity of the spiral arm matches that of the central ring, more closely than it matches the gas metallicity in the intermediate region. This suggests that gas from the spiral arm flows inward to fuel the central ring. If this process occurs very rapidly, it would prevent significant metal enrichment in the intermediate regions prior to the accumulation of gas in the nuclear ring, as suggested by A. Bittner et al. (2020).

All of these pieces of evidence indicate that gas is driven by the bar from the spiral arm into the central ring, fueling the star formation in the central ring.

Furthermore, in previous research, it has been found that bar-driven inflows can create a gas reservoir in the center of a galaxy (L. A. Silva-Lima et al. 2022). This suggests that the gas inflow driven by the bar could be the source of the gas and dust reservoir that we see in the nuclear ring (in optical and IR), which in turn may be an important fuel source for the AGN. It is also possible that the central ring may fuel the AGN in other ways, such as the ring collapse scenario described by K. Wada (2004). However, in this galaxy we currently see no explicit movement of gas between the central ring and the AGN. For a full understanding of the feeding of this AGN, especially in regards to the movement of gas in the central region, further study at higher spatial resolution is required.

As described in the Section 1, circumnuclear star-forming rings are often found in barred spiral galaxies (L. M. Mazzuca et al. 2008). They are thought to form due to inflowing gas, driven by the bar, being caught in an inner Lindblad resonance. Due to the evidence we have found supporting the dynamics of

this galaxy being dominated by bar-driven gas inflows, this seems to be the most likely origin of the central ring that we see in NGC 5806.

### 5.4. Average Stellar Population

The central ring has been established as a location of star formation; however, when we calculate the average stellar population, we find surprising results. In the central ring and spiral arm, both areas dominated by star formation, the average stellar age is relatively old and the stellar metallicity seems to be relatively low; comparatively, in the AGN-dominated central and intermediate regions, we tentatively find that the stellar age is younger and the stellar metallicity is higher. This runs counter to what would be expected in regions of star formation, and findings in similar active galaxies, e.g., J. H. Costa-Souza et al. (2024).

These results could indicate that the structure of this galaxy has been present for a long time, and thus the circumnuclear ring and spiral arm have had time to create older stars. It could also suggest that these regions saw higher rates of star formation in the past. One possible explanation for the higher stellar metallicity in the intermediate region is the slightly elevated gas metallicity in this area. Therefore, the counter-intuitive stellar population could be linked to the movement of gas within this galaxy, and thus the feeding and feedback of the AGN.

### 6. Conclusions

We have mapped the gas emission, dynamics, emission line ratios, and average stellar population properties in the central $8 \times 8 \, \mathrm{kpc}^2$ of the active galaxy NGC 5806.

We confirm that NGC 5806 has an active galactic nucleus, which is photoionizing gas over a wide range of galactic radii. The central region of this galaxy, with a projected radius of about 400 pc, is shown in a BPT diagram to be dominated by an AGN, and shows strong, extended [O III] emission. In this region, we also find a high gas velocity dispersion, up to $90 \, \mathrm{km \, s}^{-1}$, and gas metallicity close to solar metallicity.

Outside of this region, NGC 5806 has a central ring with strong ionized gas emission, which we identify as a star-forming region using the BPT diagram. Despite the presence of star formation, we tentatively find that the average stellar population of this ring is relatively old and low metallicity when compared to the stellar population of the rest of the galaxy. The gas metallicity in this ring matches that of the outer spiral arm, supporting a scenario of gas inflow from the spiral arm to the central ring. This inflow is also evidenced by the high gas velocity dispersion in the northeast portion of this ring. When viewing emission line fluxes, the central ring appears to have a gap in the northeast. It is likely that this gap is caused by a dust lane blocking the observer's view of the ring, but star formation may also be reduced in this location due to the inflow of gas from the bar.

In the intermediate region, between the central ring and the spiral arm, we have found surprisingly far-reaching AGN-dominated gas excitation. We find AGN-dominated gas emissions throughout the intermediate region, extending up to ~3.5 kpc away from the center of the galaxy. We have also shown that this region has slightly higher gas and stellar metallicity than the central ring and the spiral arm. The velocity

dispersion of both gas and stars is elevated just outside the central ring.

At the edges of our image, up to 4 kpc away from the AGN, we find an H II region in NGC 5806's spiral arm. This arm's kinematics match the disk around it, and it is has strong, clumpy ionized gas emission. The gas metallicity of this spiral arm is near solar values, and matches the gas metallicity of the central ring.

When looking at the galaxy overall, we have shown that the dynamics are dominated by the presence of a galactic bar. The bar drives gas from the spiral arm into the circumnuclear ring, fueling star formation. We find no evidence of AGN-driven gas outflows, despite the far-reaching AGN-dominated gas excitation. We also see, in the macroscopic view of this galaxy, that the gas is mostly concentrated in the spiral arm and the central ring.

We chose to analyze NGC 5806 in order to observe how an AGN interacts with its host galaxy. In answer to this question, we find AGN-dominated gas excitation in the center of the galaxy, and also reaching over 3 kpc away from the AGN. We also find high stellar and gas velocity dispersion in the very nucleus of the galaxy, potentially driven by the AGN but unresolved in our data. We observe that despite how far the influence of the AGN extends, AGN feedback does not prevent star formation in the central ring. We find unexpected results regarding the average age and metallicity of stars, which may or may not be affected by the AGN. Lastly, we find ways in which the galaxy may affect the AGN: the dynamics of this galaxy are dominated by the bar, rather than the AGN, and this bar drives gas toward the center of the galaxy, creating a circumnuclear ring that may feed the AGN.

### ORCID iDs

Sophie L. Robbins ⓘ https://orcid.org/0000-0002-4735-8494
Sandra I. Raimundo ⓘ https://orcid.org/0000-0002-6248-398X
Matthew A. Malkan ⓘ https://orcid.org/0000-0001-6919-1237

### References

Asplund, M., Grevesse, N., Sauval, A. J., & Scott, P. 2009, ARA&A, 47, 481
Bacon, R., Accardo, M., Adjali, L., et al. 2010, Proc. SPIE, 7735, 773508
Baldwin, J. A., Phillips, M. M., & Terlevich, R. 1981, PASP, 93, 5
Bennert, V. N., Treu, T., Ding, X., et al. 2021, ApJ, 921, 36
Bittner, A., Sánchez-Blázquez, P., Gadotti, D. A., et al. 2020, A&A, 643, A65
Byrne, L., Faucher-Giguère, C.-A., Stern, J., et al. 2023, MNRAS, 520, 722
Cappellari, M. 2023, MNRAS, 526, 3273
Cappellari, M., & Copin, Y. 2003, MNRAS, 342, 345
Carollo, C. M., Stiavelli, M., & Mack, J. 1998, ApJ, 116, 68
Carollo, C. M., Stiavelli, M., Seigar, M., de Zeeuw, P. T., & Dejonghe, H. 2002, AJ, 123, 159
Carvalho, S. P., Dors, O. L., Cardaci, M. V., et al. 2020, MNRAS, 492, 5675
Choi, W., Liu, L., Bureau, M., et al. 2023, MNRAS, 522, 4078

Cole, D. R., Debattista, V. P., Erwin, P., Earp, S. W. F., & Roškar, R. 2014, MNRAS, 445, 3352

Connolly, S. D., McHardy, I. M., Skipper, C. J., & Emmanoulopoulos, D. 2016, MNRAS, 459, 3963

Costa-Souza, J. H., Riffel, R. A., Dors, O. L., Riffel, R., & da Rocha-Poppe, P. C. 2024, MNRAS, 527, 9192

da Silva, P., Menezes, R. B., Steiner, J. E., & Fraga, L. 2020, MNRAS, 496, 943

den Brok, M., Carollo, C. M., Erroz-Ferrer, S., et al. 2020, MNRAS, 491, 4089

Dumas, G., Mundell, C. G., Emsellem, E., & Nagar, N. M. 2007, MNRAS, 379, 1249

Elias de la Rosa, N., Benetti, S., Navasardyan, H., et al. 2004, IAUC, 8376, 2

Erroz-Ferrer, S., Carollo, C. M., den Brok, M., et al. 2019, MNRAS, 484, 5009

Fabian, A. C. 2012, ARA&A, 50, 455

Ferrarese, L., & Merritt, D. 2000, ApJL, 539, L9

Fukuda, H., Habe, A., & Wada, K. 2000, ApJ, 529, 109

Gadotti, D. A., Bittner, A., Falcón-Barroso, J., et al. 2020, A&A, 643, A14

Gebhardt, K., Bender, R., Bower, G., et al. 2000, ApJL, 539, L13

Genzel, R., Lutz, D., Sturm, E., et al. 1998, ApJ, 498, 579

Gonneau, A., Lyubenova, M., Lançon, A., et al. 2020, A&A, 634, A133

Häring, N., & Rix, H.-W. 2004, ApJL, 604, L89

Harutyunyan, A. H., Pfahler, P., Pastorello, A., et al. 2008, A&A, 488, 383

Hicks, E. K. S., Davies, R. I., Maciejewski, W., et al. 2013, ApJ, 768, 107

Hunt, L. K., & Malkan, M. A. 1999, ApJ, 516, 660

Kauffmann, G., Heckman, T. M., Tremonti, C., et al. 2003, MNRAS, 346, 1055

Kennicutt, R. C., Jr. 1998, ARA&A, 36, 189

Kewley, L. J., Dopita, M. A., Sutherland, R. S., Heisler, C. A., & Trevena, J. 2001, ApJ, 556, 121

Kewley, L. J., Groves, B., Kauffmann, G., & Heckman, T. 2006, MNRAS, 372, 961

López-Cobá, C., Sánchez, S. F., Lin, L., et al. 2022, ApJ, 939, 40

Lu, K.-X., Zhao, Y., Bai, J.-M., & Fan, X.-L. 2019, MNRAS, 483, 1722

Marconi, A., & Hunt, L. K. 2003, ApJL, 589, L21

Marino, R. A., Rosales-Ortega, F. F., Sánchez, S. F., et al. 2013, A&A, 559, A114

Mazzuca, L. M., Knapen, J. H., Veilleux, S., & Regan, M. W. 2008, ApJS, 174, 337

Neumann, J., Thomas, D., Maraston, C., et al. 2021, MNRAS, 508, 4844

Osterbrock, D. E., & Ferland, G. J. 2006, Astrophysics of Gaseous Nebulae and Active Galactic Nuclei (Mill Valley, CA: Univ. Science Books)

Raimundo, S. I., Davies, R. I., Canning, R. E. A., et al. 2017, MNRAS, 464, 4227

Raimundo, S. I., Vestergaard, M., Koay, J. Y., et al. 2019, MNRAS, 486, 123

Riffel, R. A., Storchi-Bergmann, T., Dors, O. L., & Winge, C. 2009, MNRAS, 393, 783

Salo, H., & Laurikainen, E. 2017, ApJ, 835, 252

Sellwood, J. A., & Sánchez, R. Z. 2010, MNRAS, 404, 1733

Sellwood, J. A., & Spekkens, K. 2015, arXiv:1509.07120

Seth, A., Agüeros, M., Lee, D., & Basu-Zych, A. 2008, ApJ, 678, 116

Silva-Lima, L. A., Martins, L. P., Coelho, P. R. T., & Gadotti, D. A. 2022, A&A, 661, A105

Somerville, R. S., Hopkins, P. F., Cox, T. J., Robertson, B. E., & Hernquist, L. 2008, MNRAS, 391, 481

Sormani, M. C., Binney, J., & Magorrian, J. 2015, MNRAS, 449, 2421

Spekkens, K., & Sellwood, J. A. 2007, ApJ, 664, 204

Spinoglio, L., Fernández-Ontiveros, J. A., & Malkan, M. A. 2024, ApJ, 964, 117

Springel, V., Di Matteo, T., & Hernquist, L. 2005, ApJL, 620, L79

Storchi-Bergmann, T., Dors, O. L., Jr., Riffel, R. A., et al. 2007, ApJ, 670, 959

Storchi-Bergmann, T., Lopes, R. D. S., McGregor, P. J., et al. 2010, MNRAS, 402, 819

Storchi-Bergmann, T., McGregor, P. J., Riffel, R. A., et al. 2009, MNRAS, 394, 1148

Vagnozzi, A., de Pasquale, D., Guerri, F., et al. 2004, IAUC, 8375, 1

Vazdekis, A., Koleva, M., Ricciardelli, E., Röck, B., & Falcón-Barroso, J. 2016, MNRAS, 463, 3409

Vazdekis, A., Sánchez-Blázquez, P., Falcón-Barroso, J., et al. 2010, MNRAS, 404, 1639

Venturi, G., Nardini, E., Marconi, A., et al. 2018, A&A, 619, A74

Véron-Cetty, M. P., & Véron, P. 2010, A&A, 518, A10

Wada, K. 2004, in Coevolution of Black Holes and Galaxies, ed. L. C. Ho (Cambridge: Cambridge Univ. Press), 186

Westoby, P. B., Mundell, C. G., Nagar, N. M., et al. 2012, ApJS, 199, 1

Xia, J., Malkan, M. A., Ross, N. R., & Ancheta, A. J. 2018, ApJ, 869, 138